1-24-2018

Three-Dimensional Passive-Source Reverse-Time Migration of Converted Waves: The Method

Jiahang Li
University of Rhode Island, jiahang_li@my.uri.edu

Yang Shen
University of Rhode Island, yshen@uri.edu

Wei Zhang

Follow this and additional works at: https://digitalcommons.uri.edu/gsofacpubs

Three-Dimensional Passive-Source Reverse-Time Migration of Converted Waves: The Method

RESEARCH ARTICLE

Key Points:
- Three-dimensional passive-source reverse-time migration has an advantage in imaging complex discontinuity structures
- This paper proposes new computational approaches that address several issues in previous 2-D passive-source reverse-time migration
- Our method uses the spherical coordinate, which is well suited for solving regional and global problems

Supporting Information:
- Supporting Information S1

Correspondence to:
J. Li,
jiahang_li@my.uri.edu

Three-Dimensional Passive-Source Reverse-Time Migration of Converted Waves: The Method

Jiahang Li[1] [iD], Yang Shen[1], and Wei Zhang[2]

[1]Graduate School of Oceanography, University of Rhode Island, Narragansett, RI, USA, [2]Department of Earth and Space Sciences, Southern University of Science and Technology, Shenzhen Shi, China

Abstract At seismic discontinuities in the crust and mantle, part of the compressional wave energy converts to shear wave, and vice versa. These converted waves have been widely used in receiver function (RF) studies to image discontinuity structures in the Earth. While generally successful, the conventional RF method has its limitations and is suited mostly to flat or gently dipping structures. Among the efforts to overcome the limitations of the conventional RF method is the development of the wave-theory-based, passive-source reverse-time migration (PS-RTM) for imaging complex seismic discontinuities and scatters. To date, PS-RTM has been implemented only in 2D in the Cartesian coordinate for local problems and thus has limited applicability. In this paper, we introduce a 3D PS-RTM approach in the spherical coordinate, which is better suited for regional and global problems. New computational procedures are developed to reduce artifacts and enhance migrated images, including back-propagating the main arrival and the coda containing the converted waves separately, using a modified Helmholtz decomposition operator to separate the *P* and *S* modes in the back-propagated wavefields, and applying an imaging condition that maintains a consistent polarity for a given velocity contrast. Our new approach allows us to use migration velocity models with realistic velocity discontinuities, improving accuracy of the migrated images. We present several synthetic experiments to demonstrate the method, using regional and teleseismic sources. The results show that both regional and teleseismic sources can illuminate complex structures and this method is well suited for imaging dipping interfaces and sharp lateral changes in discontinuity structures.

1. Introduction

The method of stacking receiver functions at the common conversion points (CCP) (e.g., Abe et al., 2011; Dueker & Sheehan, 1997; Ryberg & Weber, 2000; Shen et al., 1998) has been widely used to image velocity discontinuity interfaces of the Earth's interior, such as the Moho discontinuity and mantle transition zone boundaries (e.g., Ai et al., 2007; Gao & Liu, 2014; Kind et al., 2012; Rondenay et al., 2000; Tauzin et al., 2013). Stacking of multiple receiver functions over finite lateral and depth dimensions is necessary to enhance the signals of the converted waves as individual receiver functions often have low signal-to-noise ratios. Because of this spatial averaging, the CCP method assumes locally horizontal or subhorizontal velocity discontinuity interfaces within the common conversion patch (point) used in stacking (Dueker & Sheehan, 1997) and does not account for the effects of wave diffraction and scattering caused by lateral variations in the interfaces (Chen et al., 2005a). Consequently, the CCP method is inadequate for imaging complex structures such as scatters, sharp changes in discontinuity structures, and high-angle dipping or faulted interfaces (e.g., vertical Moho offsets or slabs), as demonstrated by Sheehan et al. (2000) and Cheng et al. (2016).

Several other techniques have been developed to use converted waves recorded by seismic arrays to image crustal and mantle discontinuity structures: Bostock et al. (2001) developed a 2-D imaging method using an inverse scattering theory based on generalized radon transform; Liu and Levander (2013) used generalized transform based on Kirchhoff approximation; Poppeliers and Pavlis (2003a, 2003b) used plane wave decomposition to transform the recorded data set into ray parameter and back azimuth domain plane waves and migrated them separately; Ryberg and Weber (2000) introduced poststack migration of receiver functions; Revenaugh (1995), Sheehan et al. (2000), Levander et al. (2013), and Cheng et al. (2016, 2017) developed prestack Kirchhoff migration to image scatters and velocity discontinuities; and Chen et al. (2005a, 2005b) presented a wave equation migration method, which back-propagates the CCP stacked receiver functions with one-way phase screen propagator.

Using synthetic waveforms generated by finite difference simulations, Shang et al. (2012) developed a 2-D passive-source reverse-time migration (PS-RTM) method to image complex structures with converted waves. Different from the conventional active-source, RTM method in industry (Baysal et al., 1983; Chang & McMechan 1987, 1994; McMechan, 1983), which uses both the source-side (forward) and receiver-side (time-reverse, back-propagated) wavefields, the PS-RTM method uses only the receiver-side wavefield. Therefore, as in receiver function studies, the PS-RTM images the structures beneath the receivers using converted waves without a detailed knowledge of the sources. By comparing the CCP and PS-RTM results for a synthetic model with an offset in the Moho structure, Shang et al. (2012) demonstrated the advantage of this wave equation-based migration method in imaging complex structures. Compared to Kirchhoff migration, the wave equation-based migration method is computationally more expensive. But for complex structures, it theoretically has advantages over Kirchhoff migration as it accounts for finite-frequency wave effects and overcomes, for example, multipathing in the propagating wavefield that may affect Kirchhoff migration. However, the 2-D PS-RTM method of Shang et al. (2012) has limited applicability for several reasons. First, it can only use linear seismic arrays with earthquakes from a narrow azimuth range in the direction of the linear array. Second, since it does not account for diffracted and scattered waves outside of the 2-D plane, its application is mostly suited to 2-D structures perpendicular to the linear seismic array. Finally, a smoothed reference model was used by Shang et al. (2012) to back-propagate seismic records in order to minimize spurious phase conversions at the interfaces in the back-propagated wavefields (see more discussion in section 2). This artificial smoothing of the velocity structure inevitably alters the wavefield near sharp velocity discontinuities and thus may introduce errors in the migrated images.

With the advance of computational power and deployment of dense three-component, areal seismic arrays, it is increasingly feasible and necessary to use wave equation-based migration methods to image the Earth structure without the locally horizontal subsurface assumption and accurately account for the effects of wave propagation in realistic 3-D heterogeneous structures. In this study, we extend the method of Shang et al. (2012) from 2D to 3D, using a 3-D finite difference elastic wave solver (Zhang et al., 2012) in the spherical coordinate, which is suited for simulating wave propagation at regional and global scales. Unlike Shang et al. (2012), we separate the main P arrival and P-to-S converted waves in both the data (time) and image (spatial) domains. This allows us to use reference models with realistic, sharp velocity discontinuity structures. We adapt a new imaging condition that maintains a consistent polarity of the converted phases for a given velocity contrast (from low-to-high or high-to-low velocities) for sources with different azimuths and incidence angles, making it more straightforward to stack images obtained from different earthquake sources. We focus on the P-to-S converted waves in this study, though S-to-P conversions can be applied in a similar way. In the following sections, we describe our new 3-D PS-RTM method and show several numerical examples to demonstrate the potentials of this method in imaging complex 3-D velocity discontinuity interfaces. Finally, we discuss its limitations, including the computational requirement, the effects of uneven and sparse station coverage, and random noise.

2. Method

2.1. Summary of the Computational Procedure

Our 3-D PS-RTM method contains the following steps:

Step 1: Separate the main P arrival and its coda containing converted S wave energy by windowing them in the data (time) domain;

Step 2: Back-propagate the time-reversed, three-component P wave seismogram and the coda containing the converted S wave separately to reconstruct two back-propagated elastic wavefields;

Step 3: Apply a modified Helmholtz decomposition operator to further isolate the P mode in the back-propagated P wavefield and S mode in the back-propagated coda wavefield, respectively, in the 3-D spatial domain;

Step 4: Apply an imaging condition using the P and S modes to generate an image. A newly developed imaging condition is adapted to maintain a consistent polarity of the converted phases for a given velocity contrast;
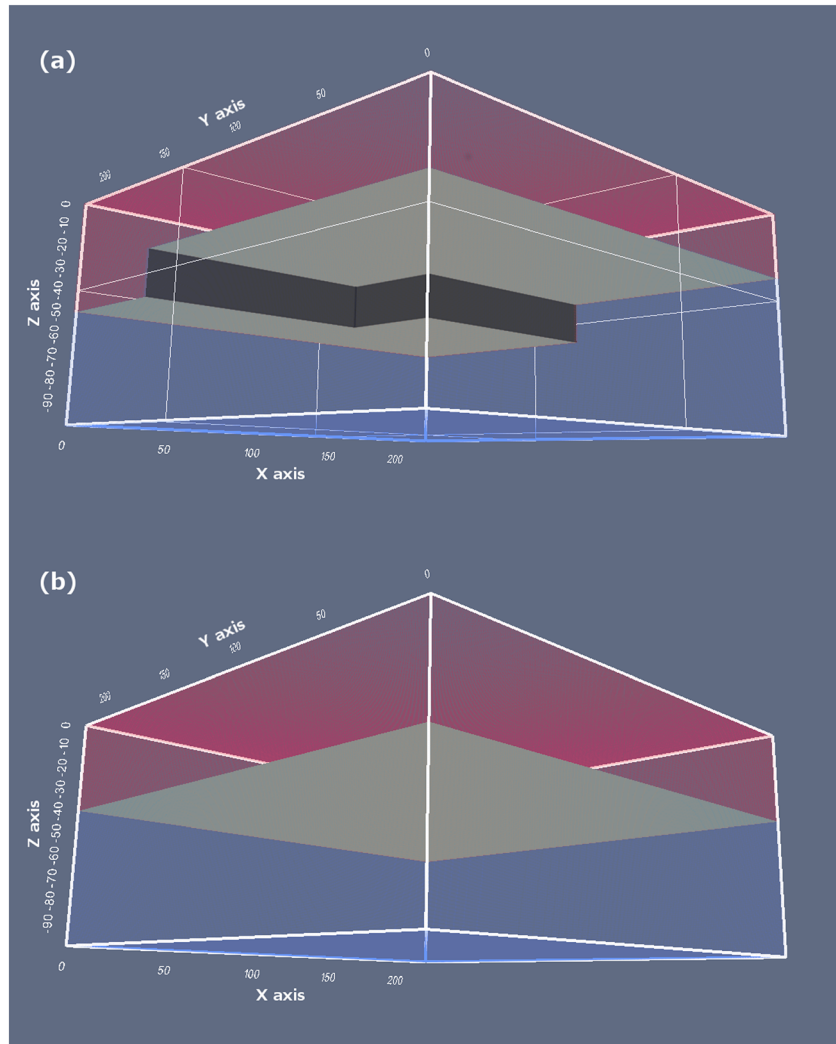
Figure 1. (a) The velocity model used to generate synthetic seismograms. It contains two layers with different *P* and *S* wave velocities as described in the text. The gray surface represents the velocity discontinuity interface between the two layers. The thin white lines outline three slices of the model at $X = 138$ km, $Y = 138$ km, and $Z = -40$ km. (b) The simplified reference velocity model used to back-propagate the recorded seismograms and image the discontinuity interfaces. The two layers have the same *P* and *S* wave velocities as in (a).

Step 5: Stack the images generated from different earthquake sources to suppress random noise and artifacts.

2.2. The Forward and Back-Propagated Wavefields

To explain the above procedure and illustrate the effects of our new approaches, we generate a 3-D synthetic model, which contains two layers with different velocities as shown in Figure 1a. The velocity interface between the two layers is offset vertically and laterally; thus, the model represents a simplified 3-D geological structure in places with vertical and lateral Moho offsets. In later discussion, we refer to the interface at 30 km depth as the shallow Moho and that at 50 km depth as the deep Moho. The dimension of this model is 222 km × 222 km laterally and 100 km in depth. The finite difference grid spacing is about 0.555 km, 0.555 km, and 0.5 km in the *x* (colatitude), *y* (longitude), and *z* (depth) directions, respectively. The upper and lower layer *S* wave velocities are 3.9 km/s and 4.4 km/s, respectively, while the *P* wave velocities are proportional to the *S* wave velocities (*Vp/Vs* = 1.74). Since the model is created in the spherical coordinate, the horizontal grid spacing decreases slightly with depth (Zhang et al., 2012).

Synthetic seismograms are calculated using the elastic wave equations with a free-surface boundary condition:

$$\rho\frac{\partial^2 \boldsymbol{u^s}}{\partial t^2} = \nabla\cdot\boldsymbol{\sigma^s}+\boldsymbol{f}, \tag{1}$$

$$\boldsymbol{\sigma^s} = \boldsymbol{c}:\boldsymbol{\varepsilon^s}, \tag{2}$$

$$\boldsymbol{\varepsilon^s} = \frac{1}{2}\left[\nabla\boldsymbol{u^s} + (\nabla\boldsymbol{u^s})^T\right], \tag{3}$$

$$\boldsymbol{\sigma^s_{xz}}(z=0) = \boldsymbol{\sigma^s_{yz}}(z=0) = \boldsymbol{\sigma^s_{zz}}(z=0) = 0. \tag{4}$$

Here $\boldsymbol{u^s}$ is the source-side (forward), three-component displacement wavefield, ρ is the density, $\boldsymbol{f}$ is the external force representing the earthquake source, $\boldsymbol{c}$ is the fourth-order stiffness tensor, $\boldsymbol{\sigma^s}$ is the stress tensor, and $\boldsymbol{\varepsilon^s}$ is the strain tensor (see details in Zhang et al., 2012). The superscript s represents the source-side variables. The subscript x, y, and z represent south, east, and up directions, respectively, in the spherical coordinate. We calculate the synthetic wavefield with a 3-D nonstaggered-grid, finite difference solver (Zhang et al., 2012) in the spherical coordinate with fourth-order spatial accuracy and second-order temporal accuracy. The free-surface condition is implemented with the stress image method (Graves, 1996; Levander, 1988), which anti-symmetrically sets the value of the stress component at ghost points above the free surface (Zhang et al., 2012). For other boundaries, we use 12 perfectly matched layers as the absorbing boundaries (Zhang & Shen, 2010).

Two types of seismic sources are used in this study: local/regional sources (Figure 2a) and teleseismic sources (Figure 2c). We save the synthetic three-component velocity seismogram on the free surface of the model with a recording length of 40 s. This recorded synthetic wavefield is used as our "data" to image the subsurface structure. Figure 2b shows an example of three-component seismograms for a regional source represented by the green star #3 in Figure 2a. Figure 2d shows an example of three-components seismograms of a plane wave with a back azimuth of 0° (due north) and an incidence angle of 27° (from the vertical, the black arrow in Figure 2c). In both examples, the main P arrival and its coda are color coded and presented on the three-component synthetic seismograms (Figures 2b and 2d). Due to the complexity of the velocity model (relative to 1-D models with flat interfaces) and the differences in the wave paths, the converted S wave arrivals have complex travel time-distance curvatures, so the moveout and stacking procedure in the CCP method will not stack the converted waves from the vertical interfaces and sharp corners effectively (Shang et al., 2012). Furthermore, since the CCP method usually uses only the radial-component receiver function for imaging purposes, it does not utilize the information provided by other components.

To construct the receiver-side elastic wavefield, we use seismograms on the evenly distributed finite difference grids on the free surface (340 by 340 grids with about 0.555 km station spacing, see section 4 for discussion on uneven and sparse station distributions), reverse the three-component seismograms in time, set them as the boundary condition on the surface of the study region, and then use the elastic wave solver of Zhang et al. (2012) to back-propagate the ground motion on the surface into the model interior by solving elastic wave equations (5)–(8):

$$\rho\frac{\partial^2 \boldsymbol{u^r}}{\partial t^2} = \nabla\cdot\boldsymbol{\sigma^r}, \tag{5}$$

$$\boldsymbol{\sigma^r} = \boldsymbol{c}:\boldsymbol{\varepsilon^r}, \tag{6}$$

$$\boldsymbol{\varepsilon^r} = \frac{1}{2}\left[\nabla\boldsymbol{u^r} + (\nabla\boldsymbol{u^r})^T\right], \tag{7}$$

$$\boldsymbol{u^r}(z=0,t) = \boldsymbol{u^s}(z=0,T-t). \tag{8}$$

These equations are similar to equations (1)–(4) except that the superscript r represents the receiver-side variables, and the free-surface boundary condition (equation (4)) is replaced with the time-reversed ground motion boundary condition (equation (8)). The external force term is removed in equation (5) because we do not add any earthquake sources for back propagation. Because the recorded data at free surface contain not only (upgoing) incident P wave but also (downgoing) converted and reflected (PS and PP) waves, we add 12 perfectly matched layers above the free surface to satisfy the condition that only the incident waves be reconstructed and back propagated into the computational grids (Sun & McMechan, 2008).
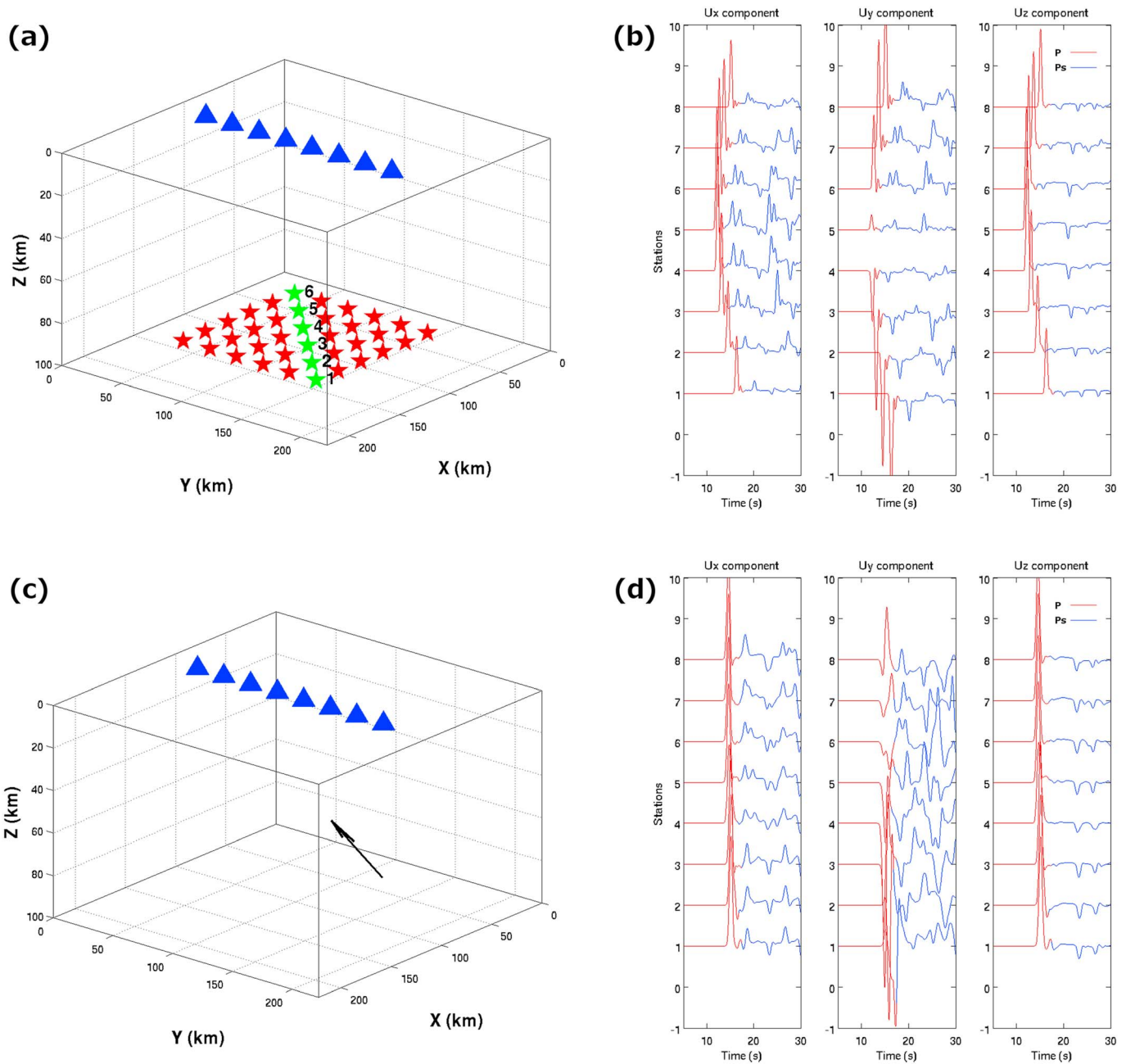
Figure 2. (a) Geometry of the sources (red and green stars) and selected stations (blue triangles) for the regional-scale synthetic experiment; (b) synthetic seismograms of source 3 recorded by the selected stations in (a). The *P* arrival and its coda are color coded as red and blue, respectively, on the three components of the seismograms. (c) Geometry of the selected stations (blue triangles) and the propagation direction of a plane wave with a back azimuth angle of 0° and incidence angle of 27° (black arrow); (d) synthetic seismograms for the plane wave and stations in (c). The *P* arrival and its coda are color coded as in (c).

The model used to back-propagate the synthetic seismograms is a simple two-layer model with an interface at 40 km depth and no vertical and lateral Moho offsets (Figure 1b). We purposefully simplify the model for back propagation from the true model but still keep a sharp velocity discontinuity in it, in contrast to the smoothed models used in Shang et al. (2012). Our goal is to demonstrate the recovery of the Moho offsets, without the artifacts of the discontinuity in the model used for back propagation.

To illustrate the possible artifacts in the back-propagated wavefield and the reason for separating the main *P* arrival and its coda in our new approach, we first back-propagate the entire time-reversed wave train,
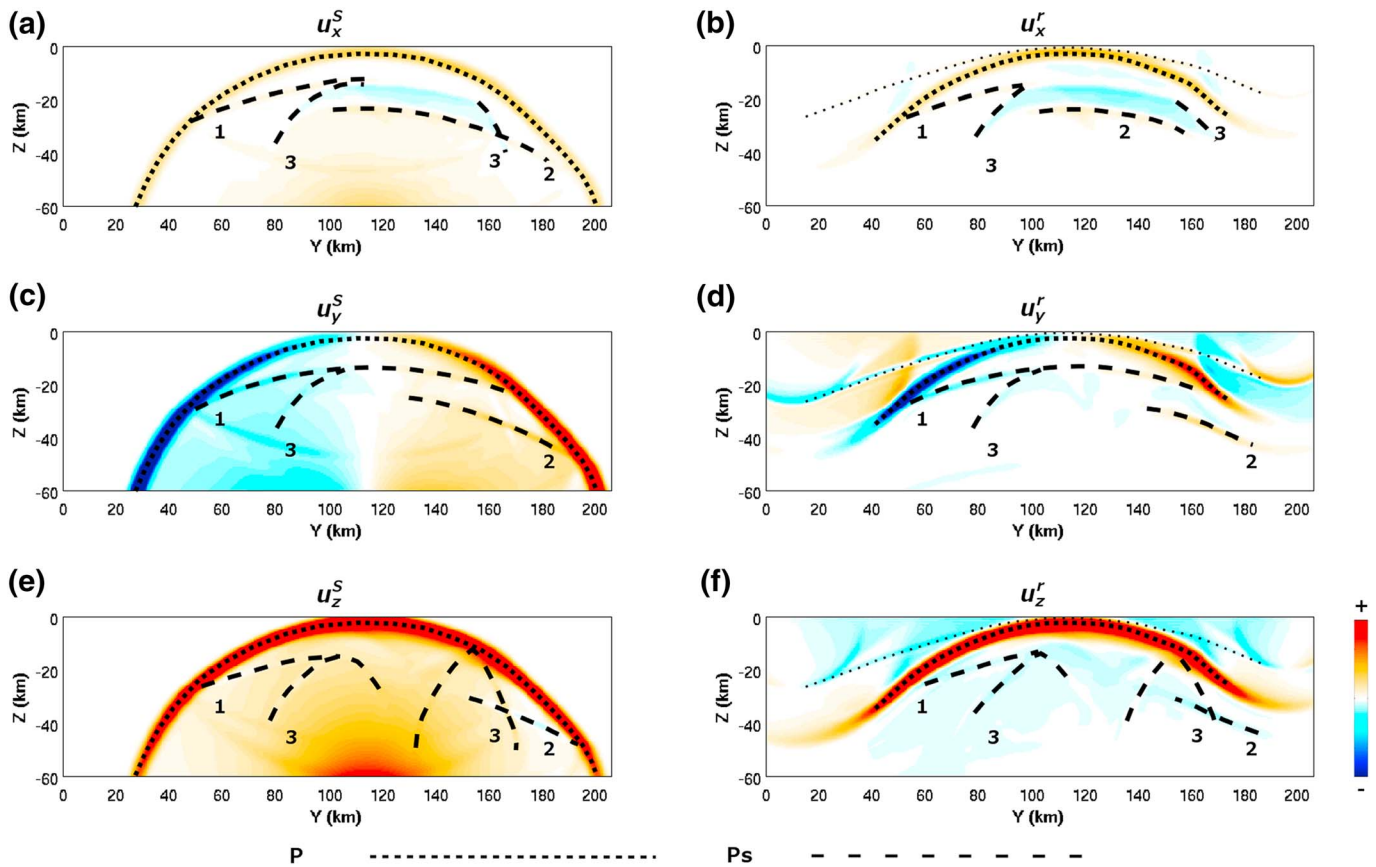
Figure 3. A snapshot at time = 12.3 s on a vertical slice across the middle of the model (at x = 111 km) of the forward (left panels: a, c, and e) and backward (right panels: b, d, and f) propagated wavefields for source 3 in Case 1 (see Figure 2). The reconstructed wavefield is obtained by back propagating the entire recorded seismic wave. The rows represent the different components of the displacement wavefield (from the top to bottom, the x, y, and z component, respectively). The converted wave from the shallow Moho (at 30 km depth) is marked as number 1; the converted wave from the deep Moho (at 50 km depth) is marked as number 2; the converted wave from the vertical interfaces is marked as number 3. The artifact caused by the incomplete boundary condition is marked with a thin dash line.

including the main arrival (P) and its coda, as in Shang et al. (2012). Figure 3 shows the snapshots at time = 12.3 s of the three-component forward and backward propagated wavefields. The converted wave generated from the shallow Moho (at 30 km depth), deep Moho (at 50 km depth), and vertical interfaces are identified and marked as thick black dashed lines 1, 2, and 3, respectively in Figure 3. By comparing the forward and backward propagated wavefields (left and right panels in Figure 3, respectively), we can also identify artifacts in the receiver-side wavefield that could contaminate the separation of the P and S modes and construction of the subsurface images.

These artifacts can be attributed to two causes. First, when we numerically back-propagate P wave (or S wave), it also generates artificial, lower amplitude S wave (or P wave), because the corresponding stress field on the surface is not recorded (Ravasi & Curtis, 2013a, 2013b) and thus the boundary condition is incomplete. The artifact related to the direct P is small in amplitude compared to the direct P wave but comparable to the converted S wave (see the thin dotted line in Figure 3d and the white dash line A in supporting information Figure S1b). Second, when we use a reference velocity model with discontinuity interfaces to back-propagate the recorded waves, the resulting waves generate spurious reflected and converted waves at the interfaces, which do not exist in the forward wavefield (black dash line B in supporting information Figure S1b). This artifact, if not removed, results in discontinuity interfaces in the RTM images that are inherited from the reference velocity model (white dash line in supporting information Figure S1c). Finally, when the P coda contains multireflected P waves, such as Pp_mP (P wave reflected at the free surface and the Moho), these phases will be back-propagated together with the converted S wave, complicating the interpretation.

2.3. Isolating P and S Modes (Steps 1–3)

To solve the problems identified in the above section, we propose several new computational approaches in the data and image domains. In the data domain, similar with Witten and Shragge (2015), we separate the three-component seismograms into the main P arrival and its time-windowed coda that contains the expected converted S wave (Figures 2b and 2d). In the seismogram examples shown, the P wave window is from the beginning of the seismograms to 2 s after the peak of the direct P arrival; the coda wave window is from the end of the P wave window to the end of the seismograms. We taper the P and the coda signal at the both ends of the windows before back-propagate them separately.

We propose a modified Helmholtz decomposition operator to further isolate P and S waves in the back-propagated wavefields. In the image domain, several decomposition methods have been developed (Zhang & McMechan, 2010). The commonly used method to separate the P and S waves with Helmholtz decomposition is shown in equations (9) and (10) (Morse & Feshbach, 1954; Zhang & McMechan, 2010):

$$P(x,y,z,t) = \nabla \cdot \boldsymbol{u^r}(x,y,z,t), \tag{9}$$

$$\boldsymbol{S}(x,y,z,t) = \nabla \times \boldsymbol{u^r}(x,y,z,t), \tag{10}$$

where P and $\boldsymbol{S}$ are the P and S modes, respectively, $\boldsymbol{u^r}$ is the receiver-side displacement wavefield generated by integrating the velocity wavefield through time. Notice that the P mode is a scalar wavefield and S mode is a vector wavefield.

In our modified Helmholtz decomposition, the P and S mode separation is achieved with equations (11) and (12),

$$\boldsymbol{P}(x,y,z,t) = -\nabla(\nabla \cdot \boldsymbol{u^{pr}}(x,y,z,t)), \tag{11}$$

$$\boldsymbol{S}(x,y,z,t) = \nabla \times (\nabla \times \boldsymbol{u^{sr}}(x,y,z,t)), \tag{12}$$

where $\boldsymbol{u^{pr}}$ is the displacement wavefield constructed from the back-propagated main P arrival, $\boldsymbol{u^{sr}}$ is the displacement wavefield constructed from the back-propagated windowed coda waves that contains the converted S wave. Here both the P and S modes are vector wavefields and the particle motions are consistent with the original P and S waves.

Figure 4 shows the P and S mode wavefields, obtained by separating the direct P wave and converted S wave in the data domain (Figures 2b and 2d), back-propagating them separately and extracting them with modified Helmholtz decomposition. Compared to the receiver-side displacement wavefield from back-propagation of the entire wave train (Figures 3b, 3d, and 3f), the artifacts are removed in the P and S modes (Figure 4). We note that the results of our modified Helmholtz decomposition (equations (11) and (12)) resemble particle acceleration with side lobes on both sides of the main peak. For imaging purpose, it does not affect the location of the main peak, and thus, it would not alter the location of the interface in the image. More complex Helmholtz operators preserving the original physical units, phase, amplitude and vector characteristics (Brytik et al., 2011; Zhang & McMechan, 2010) are computationally more expensive and beyond the scope of this paper. Since we use modified Helmholtz decomposition to isolate the S mode in the back-propagated coda wavefield, we also suppress the multiple reflections of P wave in the coda (e.g., Pp_mP).

2.4. Imaging (Steps 4 and 5)

With traditional Helmholtz decomposition (equations (9) and (10)), the conventional imaging condition (Duan & Sava, 2015) is

$$I_{ni}(x,y,z) = \int_0^T P_n(x,y,z,t;n)\,\boldsymbol{S}_{ni}(x,y,z,t;n)dt, \tag{13}$$

$$I_i^{total}(x,y,z) = \sum_{n=1}^{n_{src}} I_{ni}(x,y,z). \tag{14}$$

Here n is the index of seismic sources, n_{src} is the total number of sources, and i is x, y, or z component. P and $\boldsymbol{S}$ are the P mode and S mode obtained with traditional Helmoholtz decomposition. I_{ni} is the i component image generated with an individual source n, and I_i^{total} is the i component image after stacking images from all sources. For each source, the zero-offset cross correlations of different components of the P mode and different components of the S mode are calculated at each point in the image domain (equation (13)). Then the images of different sources are stacked to generate the finial image (equation (14)). Notice that
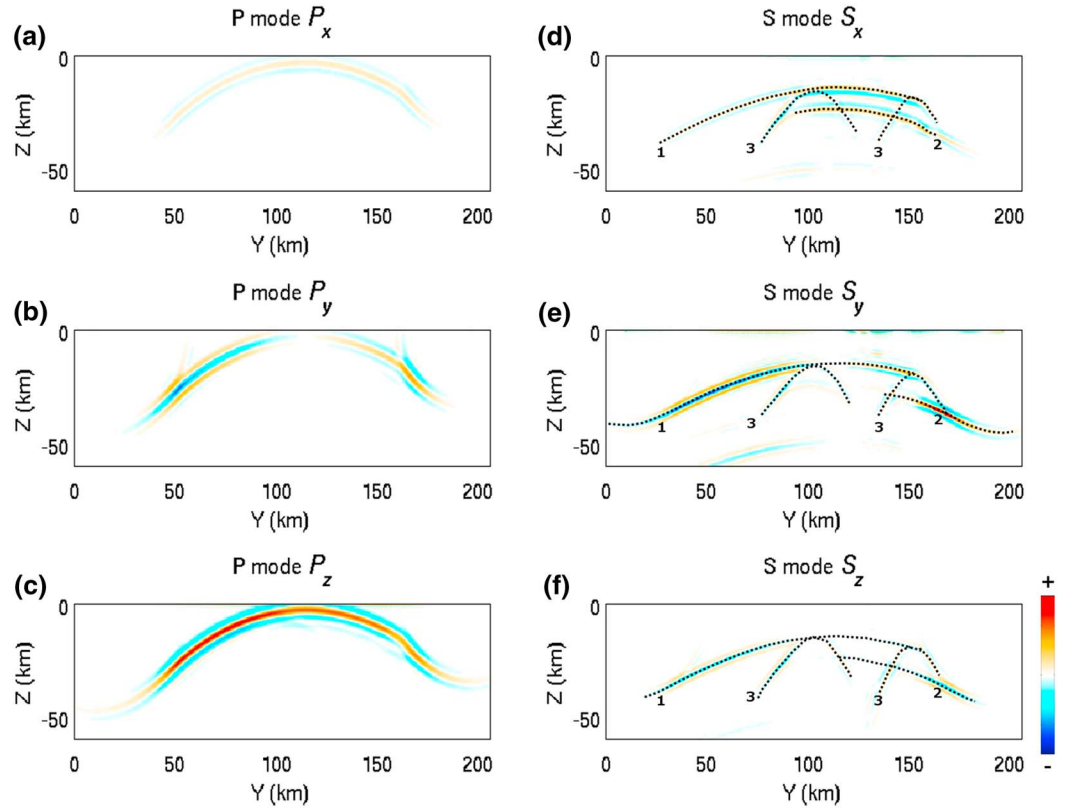
Figure 4. A snapshot at time = 12.3 s on a vertical slice across the middle of the model (at x = 111 km) of the P (left panels) and S (right panels) mode wavefields for source 3 in Case 1, obtained by back-propagating the direct P wave and P coda separately. Different rows from the top to bottom represent the x, y, and z components, respectively. The color scales for the two columns are normalized. The converted waves from the shallow and deep Moho interfaces (marked as 1 and 2, respectively) and the vertical interfaces (marked as 3) can be clearly identified in the S mode wavefield. Notice the differences in the curvatures of the converted phases from the flat Moho (1 and 2) and the vertical interfaces (3).

the conventional S mode is a vector wavefield (equation (10)) and the conventional P mode is a scalar wavefield (equation (9)), so equations (13) and (14) result in three images for the three components, which may lead to difficulties in geological interpretation (Duan & Sava, 2015). Furthermore, this imaging condition can result in the change of the polarity of the S mode at the normal incident point, which may cause destructive contributions to the stacked migrated result from difference sources (Duan & Sava, 2015; Wang et al., 2015; Figure 5).

To overcome these issues, we use the modified Helmholtz decomposition operator (equations (11) and (12)), which preserves the particle motion direction, and apply a new imaging condition:

$$I_n(x, y, z) = \int_0^T \text{sign}(\boldsymbol{P}_n(x, y, z, t; n) \cdot \boldsymbol{S}_n(x, y, z, t; n)) \cdot |\boldsymbol{P}_n(x, y, z, t; n)| \cdot |\boldsymbol{S}_n(x, y, z, t; n)| \, \text{dt}, \tag{15}$$

$$I^{\text{total}}(x, y, z) = \sum_{n=1}^{n_{\text{src}}} I_n(x, y, z) \cdot w_n. \tag{16}$$

Here $\boldsymbol{P}$ and $\boldsymbol{S}$ are the P mode and S mode obtained with modified Helmholtz decomposition (equations (11) and (12)). I_n is the image generated with an individual source n and I^{total} is the image after stacking images from all sources. w_n is the weight of nth image that can be determined by the quality of the image (such as the signal-to-noise ratio and maximum amplitude of the image).

Following Wang et al. (2015), we use the sign of the dot product of the P and S modes to correct the polarity of the image, as it maintains the polarity on both sides of the normal incident point for a given velocity contrast (from low-to-high velocities or high-to-low velocities). However, for incoming P waves with small incident angles, such as teleseismic arrivals, the dot product of the P and S modes is close to zero. So unlike in Wang et al. (2015), we use the product of the absolute P and S modes to preserve the magnitude of the
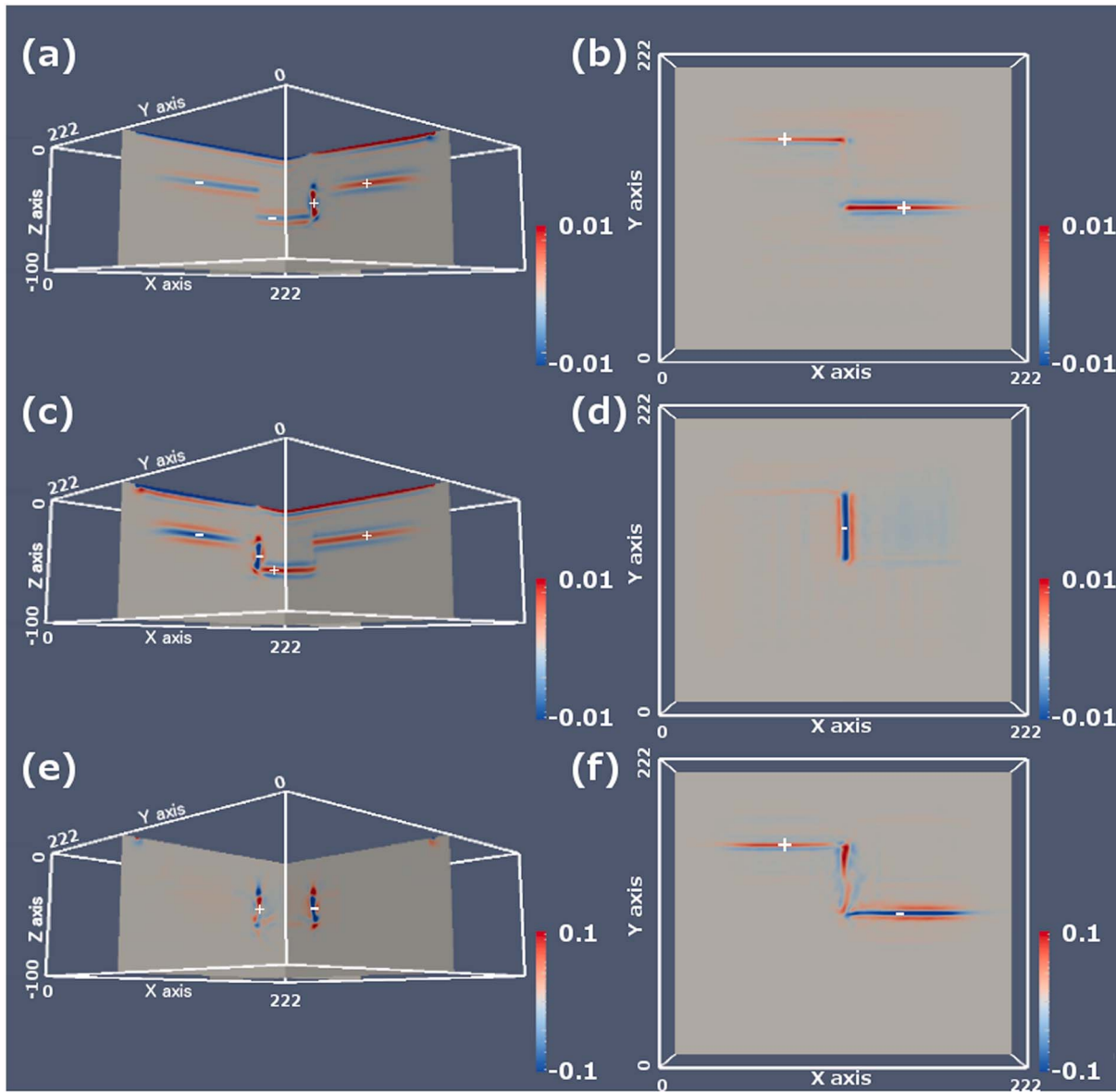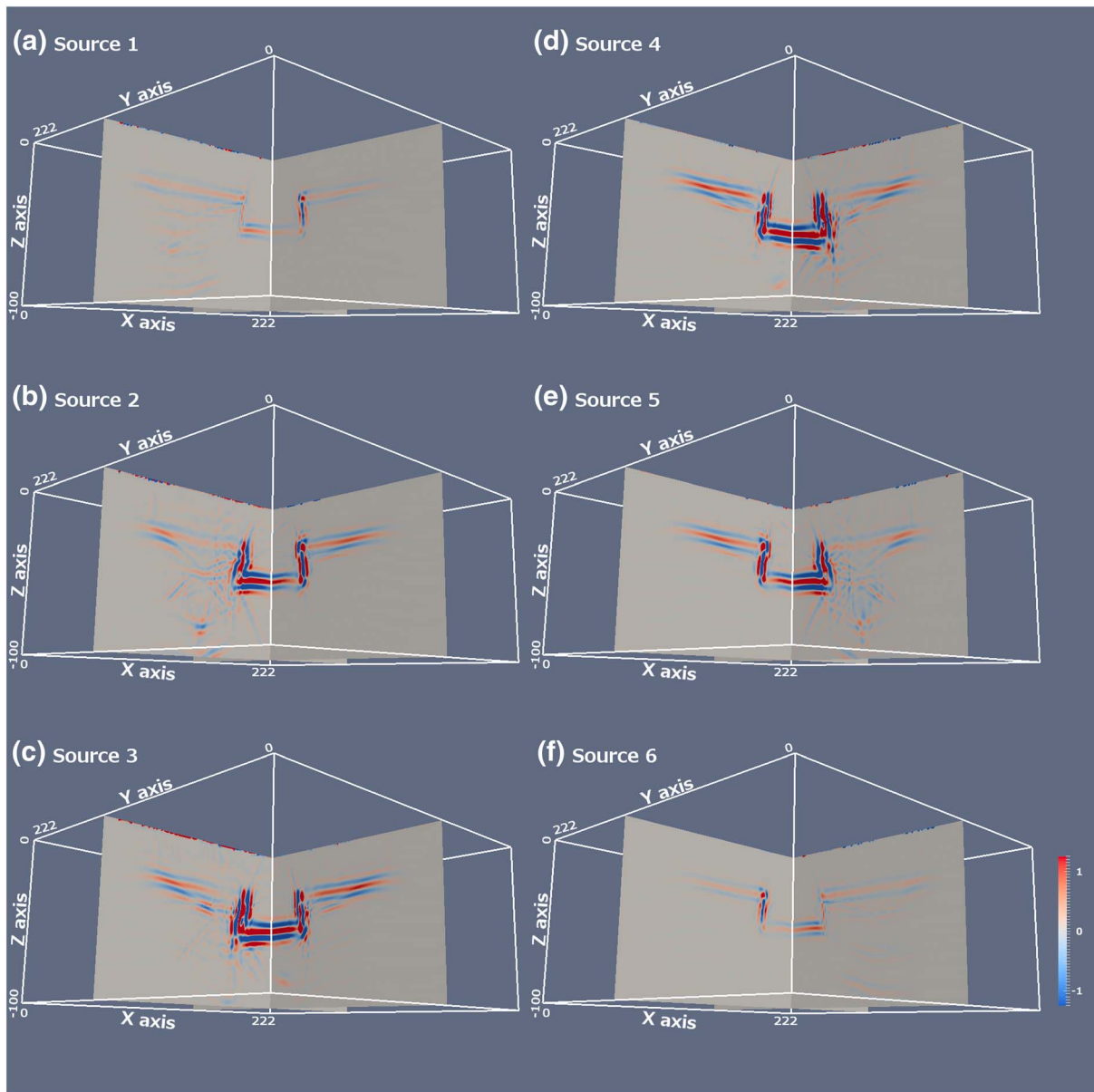
Figure 5. Results obtained with the conventional imaging condition (equations (13) and (14)). (a), (c), and (e) show the images on the vertical slices $X = 138$ km and $Y = 138$ km, while (b), (d), and (f) show the map view of the images on the horizontal slice $Z = 40$ km. (a) and (b) are the result from the P mode and the x component of the S mode; (c) and (d) are the result from the P mode and the y component of the S mode; (e) and (f) are the result from the P mode and the z component of the S mode. Notice the change in the polarity of the image at different locations of the discontinuity.

converted phase. This imaging condition creates one image instead of three, because the product of the absolute P and S modes is a scalar instead of a vector (Wang et al., 2015). After that we normalize individual images with different weights based on the quality of the images, and stack the normalized images of different sources to generate our final image with equation (16). In the synthetic tests, we use the reciprocal of the maximum amplitude of the image as the weight. For real applications, the weights depend on the noise level and illumination of the structure by seismic sources.

3. Numerical Examples

### 3.1. Model With the Moho Offset

We use the same velocity model introduced in the Method section (Figure 1a) to demonstrate the results of the 3-D PS-RTM method. In this example, we run two synthetic experiments using two types of sources. In the

Figure 6. Results obtained with the modified imaging condition (equation (15)) for the six difference sources marked in Figure 2a. The two vertical slices are at X = 138 km and Y = 138 km as outlined in Figure 1a.

first experiment (Case 1), we use deep regional sources in the model (Figure 2a), which may represent deep earthquakes in a subduction zone setting, to illuminate the study region. For simplicity, we use evenly distributed explosive sources with a Gaussian source time function having a central frequency of ~1 Hz. The sources are located at 90 km depth and have the same magnitude. In the second experiment (Case 2), we use plane waves with the incidence angle ranging from 12 to 27°, the back azimuth angle from 0 to 360° (Figure 2c), and a central frequency of ~1 Hz. Since a plane wave is an approximation for teleseismic arrivals, this experiment represents the case of using teleseismic sources with different epicentral distances and back azimuths. The simplification of the sources is justifiable as a source-equalization and deconvolution step can be applied to real earthquake data to remove the source effects.

In Case 1, the results obtained with the new imaging condition (equations (15) and (16)) and the background model in Figure 1b for back-propagation for six different sources (green stars in Figure 2a) are presented in Figure 6, showing that different parts of the model are illuminated by the different sources.
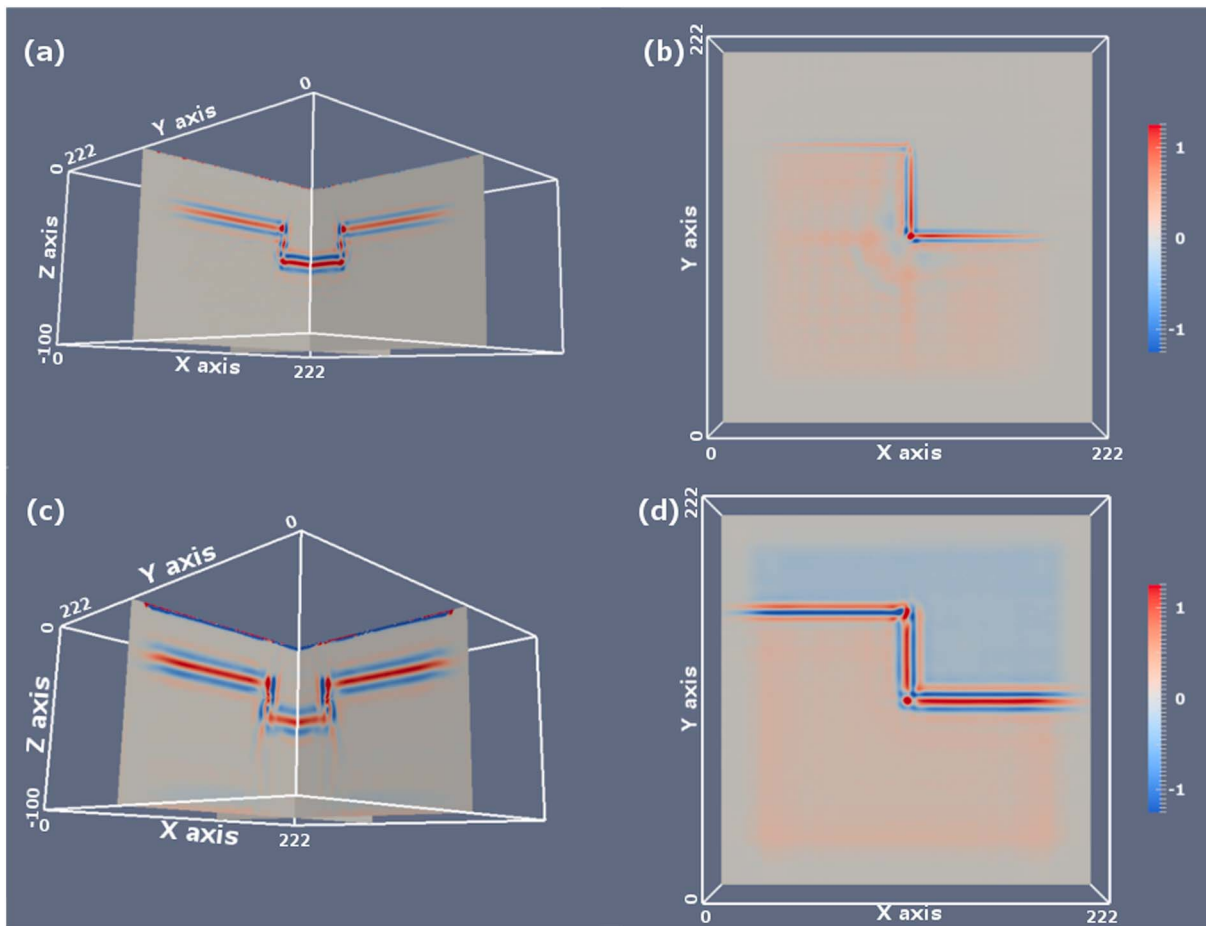
Figure 7. (a) and (b) are stacked images with the imaging condition of equation (16) using the sources in Case 1. (a) is the image result on the two vertical slices $X = 138$ km and $Y = 138$ km as outlined in Figure 1a; (b) is the image result on the horizontal slice $Z = -40$ km as outlined in Figure 1a. (c) and (d) are the same as (a) and (b) but obtained with teleseismic sources (Case 2).

For example, sources 1 and 6, which are located at the southeast and northwest corners, illuminate the southeast and northwestern parts of our model, respectively. Sources 2, 3, 4, and 5, which are located in the middle of the model, illuminate the middle part of the model. We note that the polarity of the same interfaces remains the same in all the images. After stacking all the images created with 36 different sources, the stacked image shows nearly uniform amplitude in the whole model (Figure 7a). Notice that in the horizontal slice (Figure 7b), the vertical interface at the eastern end (positive Y direction) is not well imaged, this is because the 36 sources are located near the center, so they do not provide full illumination for the vertical structure near the edge of the model, which is a limitation caused by source distribution.

In Case 2, we use 126 plane waves with different incident angles (12–27° with a 2.5° interval) and back azimuths (0–360° with a 20° interval) to represent teleseismic P arrivals to generate synthetic seismograms. This case more closely resembles receiver function studies in terms of the source-station geometry. Compared to Case 1, the whole volume of our model is well illuminated (Figure 7c) due to a larger and more complete source aperture.

For the horizontal interfaces, the polarity in the image reflects whether P wave travels from high- to low-velocity media (positive), or from low- to high-velocity media (negative). For the vertical interfaces in this model, the polarity of the interface is more complicated: the plane wave travel either from the high- to the low-velocity medium or vice versa, depending on back azimuths, so the polarity of the interface in the final stacked image depends on the majority of the converted wave record by the stations (e.g., Figure 7d).
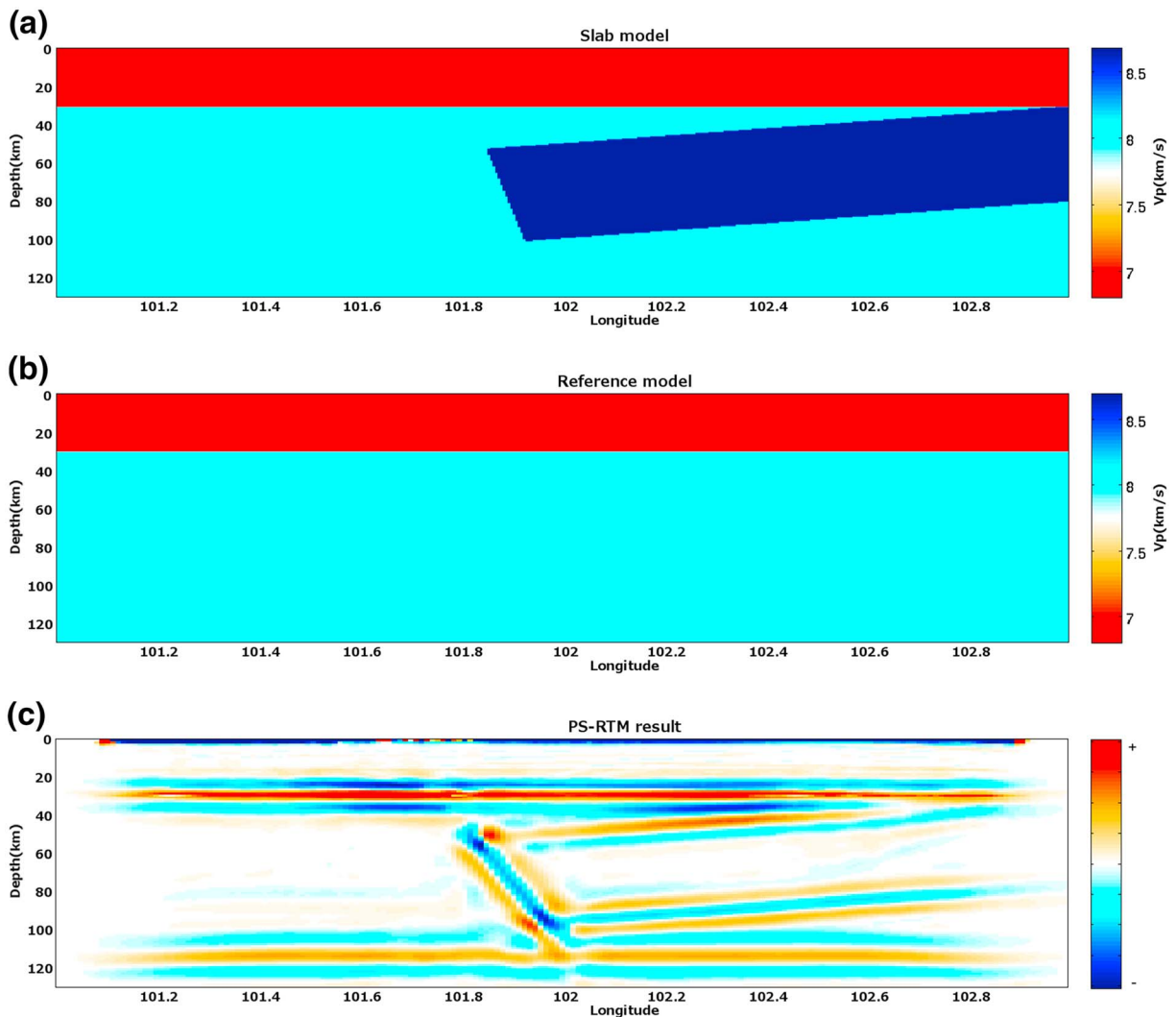
Figure 8. Image result on one vertical slice perpendicular to the strike of the subducting slab. (a) is the slab model used to calculate the synthetic seismogram; (b) is the reference model used to image the velocity discontinuities; and (c) is the 3D PS-RTM image result of the slab structure.

For the vertical interface near the model edge ($Y = 150$ km in Figure 1a), a P wave traveling in the negative Y direction enters the low-velocity layer first before it passes the vertical interface with a low- to high-velocity contrast. The converted phase from the interface is then fully recorded by the stations. For a P wave traveling in the opposite (positive Y) direction, it passes the vertical interface with a high- to low-velocity contrast, but some of the converted phase travels out of the model boundary. Thus, the converted waves from P waves from the negative Y direction likely dominate in the stack, leading to a negative-polarity interface in the migrated image (Figure 7d).

For the vertical interface near the center of the model ($Y = 111$ km), the positive polarity (Figure 7d) requires a different explanation, which we attribute to the weakening of the P wave coming from the negative Y direction at the deep Moho by reflection and conversion and then the weakening of the converted S wave at the shallow Moho by reflection and conversion. Consequently, the polarity of this interface is dominated by the P wave coming from positive Y direction, which is from high- to low-velocity medium (positive polarity).

This example shows that although the new image condition (equation (15)) can account for the polarity change on both sides of the normal incident point, care should be taken in interpreting high-dipping-angle and vertical interfaces as the sense of velocity contrast may change with back azimuths of incoming P waves and it may be necessary to stack the images by different back azimuth groups.

3.2. Subducting Slab Model

In this example, we use 126 plane waves with the same incidence angles and back azimuths as in the above teleseismic example to illuminate a slab model, which contains a homogeneous crust and a slab in an otherwise uniform upper mantle (Figure 8a). The crust and the background mantle S wave velocities are 3.900 km/s and 4.480 km/s, respectively; the corresponding P wave velocities are 6.800 km/s and 8.036 km/s, respectively. The slab structure has a +8% velocity perturbation compared with the background velocity. For simplicity, we only show a vertical profile perpendicular to the slab, which extends along the y direction. The reference velocity model used for back propagation has the same crust and background mantle but no slab structure (Figure 8b). The grid spacing and model dimension are the same as those in the Moho offset model.

The result shows that the PS-RTM method yields good constraints on the boundary of the slab structure (Figure 8c): the main peaks in the image match well with the velocity interfaces in the slab model. We note that the lower boundary and the edge of the slab have a negative polarity, which is consistent with the polarity of the converted waves from P wave traveling from the low-velocity, background mantle to a high-velocity slab. In contrast, the top interface of the slab has a positive polarity, like that of the Moho, as expected for the converted waves from P wave traveling from high to low velocities. Below the slab, the horizontal structure at depth of about 115 km is the multiple reflected and converted arrival PpP$_m$s (P reflected at the free surface and converted at the Moho). This example shows that the PS-RTM images based on P wave and its coda also suffer from the interference of shallow, multiple converted phases, as in P receiver functions.

4. Discussions

We demonstrate the potentials of the 3-D PS-RTM in imaging complex structures such as vertical or high-dipping angle Moho offsets and subducting slabs, though application of the method remains challenging as it requires a dense, three-component seismic network and high-performance computation.

4.1. Effects of Station Spacing

In the synthetic tests, we use the numerical grids on the surface as receivers to record the ground motion and back-propagate the wavefield. Although it is unrealistic to have such a dense station coverage over a ~200 km by 200 km area, there have been deployments designed to record spatially unaliased wavefields over smaller areas (e.g., Anderson et al., 2016). Large-N seismic array is a new trend in seismology, and we expect to see more of this kind of deployments in the future.

We note that wavefield spatial aliasing on the surface is a function of horizontal wavelengths (and thus wave frequencies and ray parameters). According to the Nyquist-Shannon sampling theorem, the wavefield can be fully reconstructed from the recorded seismograms at the stations, when the station spacing is smaller than the apparent half-wavelength on the surface. For scale, a 0.2 Hz teleseismic arrival with a ray parameter of 0.04–0.08 s/km, as used by Cheng et al. (2017), has an apparent horizontal wavelength of 62.5–125 km on the surface. Thus, arrays with station spacing less than 31 km are able to record unaliased wavefields of teleseismic arrivals at frequencies below 0.2 Hz.

To illustrate the effects of station spacing on the results of 3-D PS-RTM, we run three additional experiments of imaging the slab model, using seismic arrays with an average station spacing of 5 km, 10 km, and 15 km, respectively. For individual stations, the station spacing deviates from the average spacing by a random value with a zero mean and a standard deviation of 2.5 km, so the stations are not evenly distributed as in likely real deployments. Based on the S wave velocity of the crustal layer (3.9 km/s) and the range of incident angles of plane waves (12 to 27°), we calculate that the ray parameter is 0.053 to 0.116 s/km. For the 1 Hz plane waves used in our numerical experiments, the apparent horizontal wavelength on the surface is 8.6 to 18.8 km. Thus, the station coverages in these three additional experiments range from unaliased and slightly aliased (5 km station spacing, depending on ray parameter) to severely aliased (15 km station spacing).

We interpolate the seismograms at the stations onto the finite difference grids on the surface before we back-propagate the wavefield for two reasons. First, the stations are usually not located exactly at the finite difference grids, so interpolation is necessary to reduce the error caused by the location offsets between the stations and the grids. Second, without interpolation, the grids without stations have zero values,

resulting in a discrete and discontinuous surface boundary condition for back-propagation, which causes strong artifacts near the surface (supporting information Figure S2).

Interpolation of wavefields recorded by sparse stations is a topic of numerous studies (e.g., Hennenfent et al., 2010; Poppeliers & Pavlis, 2003a; Shang, 2014; Zhang & Zheng, 2015). In this study, we use a Delaunay triangulation of the scattered sample points (cubic spline of griddata in Matlab) to interpolate the seismograms at the stations onto the finite difference grids on the surface. We first align the P arrivals from the recording stations by waveform cross correlation and construct a corresponding map of the P travel time differences. The aligned waveforms are then interpolated by Delaunay triangulation, time step by time step, on to the surface finite difference grids. The corresponding travel time differences for the grids are calculated by triangulation of the P travel times at the stations. Finally, the interpolated waveforms on all the grids are time-shifted back using the travel time differences. The following time-reversal and back-propagation procedures remain the same.

For unaliased and weakly aliased wavefields (5 km average station spacing), the interpolation works well and the resulting image (supporting information Figure S3a) is nearly identical to that of the wavefield recorded on all the surface grids (Figure 8c). For aliased and strongly aliased wavefields (10 km and 15 km average station intervals), the steep interface at the deep end of the slab deteriorates, though the horizontal interface (the Moho) and the gently dipping upper and lower interfaces of the slab remain well imaged (supporting information Figures S3b and S3c). We attribute the differences to the relative moveout (time-distance curve/surface) between the converted phases and the P arrivals. The relative moveout is small for the converted waves from the flat and gently dipping interfaces, so waveforms on adjacent stations aligned on the P arrival are similar enough for interpolation to reconstruct the converted phases even at 10–15 km station spacing. On the other hand, the relative moveout of the converted phase from the steep interface is much larger, so the reconstruction of the converted phase by interpolation works only at small station spacing (Figure S3). Other more sophisticated interpolation methods (e.g., Hennenfent et al., 2010) that can identify and link arrivals with various moveout curves/surfaces at adjacent stations are worth exploring to improve the wavefield reconstruction in applications to real data.

4.2. Computational Consideration

The separation of the main P arrival and its coda in the data domain and their separate back-propagation to isolate the P and S modes allow us to use realistic velocity models with sharp discontinuities (Figure 7), though the trade-off is doubling of the memory requirement used in back-propagation, which leads to about four times longer computation than back-propagating the whole wave train and separating the P and S modes only in the image domain.

The computational cost of 3-D PS-RTM is generally proportional to the number of earthquakes used in imaging. In our study, calculation for each earthquake needs about 2 h wall-clock time with 40 CPU cores on a high-performance cluster at the University of Rhode Island. To calculate the wavefields of 126 teleseismic sources, we need a total of about 24 h with 400 CPU cores. Bases on this experience, we anticipate that application of 3-D PS-RTM will be feasible at regional (a few hundred kilometers to a thousand kilometers) scales in the near future, given an adequate seismic array and moderate (100s to 1,000s CPU cores) high-performance computational resources.

4.3. Random Noise

To show the effect of random noise, we present another numerical experiment, in which white noise is added to the three-component seismograms. We use the same interpolation method discussed above to interpolate the seismograms recorded by the array with 5 km average station spacing onto the numerical grids on the free surface. For seismograms with a signal-to-noise ratio of 20, or when the amplitude of noise is about the same level of the converted wave, we can clearly image the structure in the upper mantle and the Moho (Figure S4). The signal-to-noise ratio is defined as the amplitude of the direct P arrival divided by the standard deviation of the random noise. Compared to the case without added random noise (Figure S3b), the added noise introduced artifacts, most obviously in the shallow crust. The diminishing impact of random noise with depth can be understood as the superposition of increasing amount of data from an expanding Fresnel zone with depth suppresses random noise.

5. Conclusions

We have developed a 3-D PS-RTM method to image velocity discontinuities and scatters. Compared with the CCP method, this method is better suited to image complex structures (e.g., Moho offsets, sutures, and sub-ducting slabs). Our new method builds on the 2-D PS-RTM method of Shang et al. (2012) with several significant differences and improvements. First, we extend the method to 3D using a finite difference wave equation solver in the spherical coordinate (Zhang et al., 2012), so it can be applied to 3-D geological structures at regional and global scales. Second, we separate the main *P* arrival and its coda containing the converted *S* wave in the data domain and back propagate them separately. This new procedure doubles the memory requirement but suppresses the artificial converted waves generated by the discontinuities in the reference velocity model in the back-propagated wavefields, allowing us to use realistic velocity models with discontinuities. The new procedure also suppresses the multiple *P* reflections (e.g., Pp_mp) and artifacts caused by the incomplete boundary condition, though converted *P*-to-*S* phases from shallow reverberations could be falsely mapped as a deep structure, as in *P* receiver functions. We apply a modified Helmholtz decomposition operator to isolate *P* and *S* wave energy in the separate, back-propagated wavefields and then apply a new imaging condition to the *P* and *S* mode wavefields to generate images. The new image condition maintains the polarity on both sides of the normal incident point and thus yields a consistent polarity of the converted phases for a given velocity contrast (from low to high or high to low velocities) for sources with different azimuths and incidence angles, making it more straightforward to stack images obtained from earthquake sources from different azimuths and incidence angles. Though care should be taken for vertical and high-dipping angle interfaces, for which the sense of the velocity contrast may change with the back azimuths of incoming waves. Care should also be taken in the choices of wave frequencies and interpolation methods to use to reconstruct the wavefield on the surface from seismograms recorded by unevenly distributed stations, and the screening of earthquake records to minimize the effects of random noise. Application of the 3-D PS-RTM to real data sets requires high-performance computational resources.

References

Abe, Y., Ohkura, T., Hirahara, K., & Shibutani, T. (2011). Common-conversion-point stacking of receiver functions for estimating the geometry of dipping interfaces. *Geophysical Journal International*, 185, 1305–1311. https://doi.org/10.1111/j.1365-246X.2011.05001.x

Ai, Y., Chen, Q.-f., Zeng, F., Hong, X., & Ye, W. (2007). The crust and upper mantle structure beneath southeastern China. *Earth and Planetary Science Letters*, 260, 549–563. https://doi.org/10.1016/j.epsl.2007.06.009

Anderson, K. R., Woodward, R., Sweet, J. R., Bilek, S. L., Brudzinski, M., Chen, X., … Stump, B. W. (2016). Full wavefield recordings of Oklahoma seismicity from an IRIS-led community experiment. Abstract S11D–2493 Presented at the 2016 AGU Fall Meeting, San Francisco, CA.

Baysal, E., Kosloff, D. D., & Sherwood, J. W. C. (1983). Reverse time migration. *Geophysics*, 48(11), 1514–1524. https://doi.org/10.1190/1.1441434

Bostock, M. G., Rondenay, S., & Shragge, J. (2001). Multiparameter two-dimensional inversion of scattered teleseismic body waves 1. Theory for oblique incidence. *Journal of Geophysical Research*, 106(B12), 30,771–30,782. https://doi.org/10.1029/2001JB000330

Brytik, V., de Hoop, M. V., Smith, H. F., & Uhlmann, G. (2011). Decoupling of modes for the elastic wave equation in media of limited smoothness. *Communications in Partial Differential Equations*, 36, 1683–1693. https://doi.org/10.1080/03605302.2011.558554

Chang, W. F., & McMechan, G. A. (1987). Elastic reverse-time migration. *Geophysics*, 52(10), 1365–1375. https://doi.org/10.1190/1.1442249

Chang, W. F., & McMechan, G. A. (1994). 3-D elastic prestack, reverse-time depth migration. *Geophysics*, 59(4), 597–609. https://doi.org/10.1190/1.1443620

Chen, L., Wen, L., & Zheng, T. (2005a). A wave equation migration method for receiver function imaging: 1. Theory. *Journal of Geophysical Research*, 110, B11309. https://doi.org/10.1029/2005JB003665

Chen, L., Wen, L., & Zheng, T. (2005b). A wave equation migration method for receiver function imaging: 2. Application to the Japan subduction zone. *Journal of Geophysical Research*, 110, B11310. https://doi.org/10.1029/2005JB003666

Cheng, C., Bodin, T., & Allen, R. M. (2016). Three-dimensional pre-stack depth migration of receiver functions with the fast marching method: A Kirchhoff approach. *Geophysical Journal International*, 205(2), 819–829. https://doi.org/10.1093/gji/ggw062

Cheng, C., Bodin, T., Tauzin, B., & Allen, R. M. (2017). Cascadia subduction slab heterogeneity revealed by three-dimensional receiver function Kirchhoff migration. *Geophysical Research Letters*, 44, 694–701. https://doi.org/10.1002/2016GL072142

Duan, Y., & Sava, P. (2015). Scalar imaging condition for elastic reverse time migration. *Geophysics*, 80(4), S127–S136. https://doi.org/10.1190/geo2014-0453.1

Dueker, K. G., & Sheehan, A. F. (1997). Mantle discontinuity structure from midpoint stacks of converted P to S waves across the Yellowstone hotspot track. *Journal of Geophysical Research*, 102(B4), 8313–8327. https://doi.org/10.1029/96JB03857

Gao, S. S., & Liu, K. H. (2014). Mantle transition zone discontinuities beneath the contiguous United States. *Journal of Geophysical Research: Solid Earth*, 119, 6452–6468. https://doi.org/10.1002/2014JB011253

Graves, R. W. (1996). Simulating seismic wave propagation in 3D elastic media using staggered-grid finite differences. *Bulletin of the Seismological Society of America*, 86(4), 1091–1106.

Hennenfent, G., Fenelon, L., & Herrmann, F. J. (2010). Nonequispaced curvelet transform for seismic data reconstruction: A sparsity-promoting approach. *Geophysics*, 75, WB203–WB210. https://doi.org/10.1190/1.3494032

Kind, R., Yuan, X., & Kumar, P. (2012). Seismic receiver functions and the lithosphere–asthenosphere boundary. *Tectonophysics*, 536-537, 25–43. https://doi.org/10.1016/j.tecto.2012.03.005

Levander, A. R. (1988). Fourth-order finite-difference P-SV seismograms. *Geophysics*, 53(11), 1425–1436. https://doi.org/10.1190/1.1442422

Levander, A., Niu, F., & Symes, W. W. (2013). Imaging teleseismic P to S scattered waves using the Kirchhoff integral. In *Seismic Earth: Array Analysis of Broadband Seismograms* (pp. 149–169). Washington DC: American Geophysical Union. https://doi.org/10.1029/157GM10

Liu, K., & Levander, A. (2013). Three-dimensional Kirchhoff-approximate generalized Radon transform imaging using teleseismic P-to-S scattered waves. *Geophysical Journal International*, *192*(3), 1196–1216. https://doi.org/10.1093/gji/ggs073

McMechan, G. A. (1983). Migration by extrapolation of time-dependent boundary values. *Geophysical Prospecting*, *31*(3), 413–420. https://doi.org/10.1111/j.1365-2478.1983.tb01060.x

Morse, P. M., & Feshbach, H. (1954). Methods of theoretical physics. *American Journal of Physics*, *22*(6), 410–413. https://doi.org/10.1119/1.1933765

Poppeliers, C., & Pavlis, G. L. (2003a). Three-dimensional, prestack, plane wave migration of teleseismic P-to-S converted phases: 1. Theory. *Journal of Geophysical Research*, *108*(B2), 2112. https://doi.org/10.1029/2001JB000216

Poppeliers, C., & Pavlis, G. L. (2003b). Three-dimensional, prestack, plane wave migration of teleseismic P-to-S converted phases: 2. Stacking multiple events. *Journal of Geophysical Research*, *108*(B5), 2112. https://doi.org/10.1029/2001JB001583

Ravasi, M., & Curtis, A. (2013a). Elastic imaging with exact wavefield extrapolation for application to ocean-bottom 4C seismic data. *Geophysics*, *78*(6), S265–S284. https://doi.org/10.1190/geo2013-0152.1

Ravasi, M., & Curtis, A. (2013b). Nonlinear scattering based imaging in elastic media: Theory, theorems, and imaging conditions. *Geophysics*, *78*(3), S137–S155. https://doi.org/10.1190/geo2012-0286.1

Revenaugh, J. (1995). A scattered-wave image of subduction beneath the transverse ranges. *Science*, *268*(5219), 1888–1892. https://doi.org/10.1126/science.268.5219.1888

Rondenay, S., Bostock, M. G., Hearn, T. M., White, D. J., & Ellis, R. M. (2000). Lithospheric assembly and modification of the SE Canadian Shield: Abitibi-Grenville teleseismic experiment. *Journal of Geophysical Research*, *105*(B6), 13,735–13,754. https://doi.org/10.1029/2000JB900022

Ryberg, T., & Weber, M. (2000). Receiver function arrays: A reflection seismic approach. *Geophysical Journal International*, *141*(1), 1–11. https://doi.org/10.1046/j.1365-246X.2000.00077.x

Shang, X. (2014). *Inverse Scattering: Theory and Application to the Imaging of the Earth's Seismic Discontinuities*. Cambridge, MA: Massachusetts Institute of Technology.

Shang, X., de Hoop, M. V., & van der Hilst, R. D. (2012). Beyond receiver functions: Passive source reverse time migration and inverse scattering of converted waves. *Geophysical Research Letters*, *39*, L15308. https://doi.org/10.1029/2012GL052289

Sheehan, A. F., Shearer, P. M., Gilbert, H. J., & Dueker, K. G. (2000). Seismic migration processing of P-SV converted phases for mantle discontinuity structure beneath the Snake River Plain, western United States. *Journal of Geophysical Research*, *105*(B8), 19,055–19,065. https://doi.org/10.1029/2000JB900112

Shen, Y., Solomon, S. C., Bjarnason, I. T., & Wolfe, C. J. (1998). Seismic evidence for a lower-mantle origin of the Iceland plume. *Nature*, *395*(6697), 62–65. https://doi.org/10.1038/25714

Sun, R., & McMechan, G. A. (2008). Amplitude effect of the free surface in elastic reverse-time extrapolation. *Geophysics*, *73*, S177–S184. https://doi.org/10.1190/1.2953977

Tauzin, B., van der Hilst, R. D., Wittlinger, G., & Ricard, Y. (2013). Multiple transition zone seismic discontinuities and low velocity layers below western United States. *Journal of Geophysical Research: Solid Earth*, *118*, 2307–2322. https://doi.org/10.1002/jgrb.50182

Wang, C., Cheng, J., & Arntsen, B. (2015). Imaging condition for converted waves based on decoupled elastic wave modes. In *SEG Technical Program Expanded Abstracts 2015* (pp. 4385–4390). Shanghai, China: Society of Exploration Geophysicists. https://doi.org/10.1190/segam2015-5920952.1

Witten, B., & Shragge, J. (2015). Extended wave-equation imaging conditions for passive seismic data. *Geophysics*, *80*(6), WC61–WC72. https://doi.org/10.1190/geo2015-0046.1

Zhang, Q., & McMechan, G. A. (2010). 2D and 3D elastic wavefield vector decomposition in the wavenumber domain for VTI media. *Geophysics*, *75*, D13–D26. https://doi.org/10.1190/1.3431045

Zhang, W., & Shen, Y. (2010). Unsplit complex frequency-shifted PML implementation using auxiliary differential equations for seismic wave modeling. *Geophysics*, *75*, T141–T154. https://doi.org/10.1190/1.3463431

Zhang, J., & Zheng, T. (2015). Receiver function imaging with reconstructed wavefields from sparsely scattered stations. *Seismological Research Letters*, *86*(1), 165–172. https://doi.org/10.1785/0220140028

Zhang, W., Shen, Y., & Zhao, L. (2012). Three-dimensional anisotropic seismic wave modelling in spherical coordinates by a collocated-grid finite-difference method. *Geophysical Journal International*, *188*, 1359–1381. https://doi.org/10.1111/j.1365-246X.2011.05331.x